Hydrol. Earth Syst. Sci., 17, 4671–4683, 2013
www.hydrol-earth-syst-sci.net/17/4671/2013/
doi:10.5194/hess-17-4671-2013

Hydrology and Earth System Sciences
Open Access

River ice flux and water velocities along a 600 km-long reach of Lena River, Siberia, from satellite stereo

A. Kääb[1], **M. Lamare**[1], **and M. Abrams**[2]

[1]Department of Geosciences, University of Oslo, P.O. Box 1047, Oslo, Norway
[2]Jet Propulsion Laboratory/California Institute of Technology, Pasadena, CA, USA

Correspondence to: A. Kääb (kaeaeb@geo.uio.no)

Received: 24 June 2013 – Published in Hydrol. Earth Syst. Sci. Discuss.: 29 July 2013
Revised: 12 October 2013 – Accepted: 17 October 2013 – Published: 26 November 2013

Abstract. Knowledge of water-surface velocities in rivers is useful for understanding a range of river processes. In cold regions, river-ice break up and the related downstream transport of ice debris is often the most important hydrological event of the year, leading to flood levels that typically exceed those for the open-water period and to strong consequences for river infrastructure and ecology. Accurate and complete surface-velocity fields on rivers have rarely been produced. Here, we track river ice debris over a time period of about one minute, which is the typical time lag between the two or more images that form a stereo data set in spaceborne, along-track optical stereo mapping. Using a series of nine stereo scenes from the US/Japanese Advanced Spaceborne Thermal Emission and Reflection Radiometer (ASTER) onboard the NASA Terra spacecraft with 15 m image resolution, we measure the ice and water velocity field over a 620 km-long reach of the lower Lena River, Siberia, just above its entry into the Lena delta. Careful analysis and correction of higher-order image and sensor errors enables an accuracy of ice-debris velocities of up to 0.04 m s^{-1} from the ASTER data. Maximum ice or water speeds, respectively, reach up to 2.5 m s^{-1} at the time of data acquisition, 27 May 2011 (03:30 UTC). Speeds show clear along-stream undulations with a wavelength of about 21 km that agree well with variations in channel width and with the location of sand bars along the river reach studied. The methodology and results of this study could be valuable to a number of disciplines requiring detailed information about river flow, such as hydraulics, hydrology, river ecology and natural-hazard management.

1 Introduction

Measuring surface-velocity fields on rivers has been attempted for decades for scientific and applied purposes. Related water fluxes and forces lead to erosion, transport or sedimentation of matter in the river, at the riverbed or its banks, with implications for river ecology, fluvial geomorphology and human infrastructure (Kääb and Prowse, 2011). In cold regions, such needs are enlarged by effects of river ice, the break-up of which often creates the most important hydrological event of the year (Prowse, 1994, 2005). Even estimating discharge during this period and, for instance, the associated freshwater fluxes into the Arctic and circum-Arctic oceans (Peterson et al., 2002), however, is difficult and often inaccurate due to the ice disruption of hydrometric equipment and effects on stage-discharge rating curves (Shiklomanov et al., 2006; White and Beltaos, 2008). Break-up can also severely affect river ecosystems and human infrastructure, such as settlements, bridges and hydroelectric facilities (Gerard and Davar, 1995; Prowse and Culp, 2003). Of particular importance are ice-jam-generated waves that can travel rapidly downstream and be especially destructive (Jasek and Beltaos, 2008). The economic costs from break-up ice jams are estimated to average almost USD 250 million per year in North America and to have been over USD 100 million for a single 2001-event in Eastern Russia (Prowse et al., 2007). Although typically less dynamic than break-up, freeze-up can create a similar set of bio-geophysical problems on many cold-region rivers.

Overall, the monitoring, field study and modelling of river conditions during these two periods have been hampered by a lack of comprehensive water and ice velocity fields.

Airborne and orbital remote sensing offers possibilities to obtain such information over entire river reaches. Previous studies using airborne or spaceborne data investigated for instance: the potential of estimating river discharge from air and space, mainly based on remotely sensed river width and level (Smith, 1997; Bjerklie et al., 2003, 2005; Smith and Pavelsky, 2008), subtle river ice deformation (Smith, 2002; Vincent et al., 2004) using radar interferometry; river ice properties and density from radar imagery (Mermoz et al., 2009; Unterschultz et al., 2009); river currents using airborne and spaceborne along-track radar interferometry (Siegmund et al., 2004; Bjerklie et al., 2005; Romeiser et al., 2007, 2010).

The time lag or the related angular difference between along-track stereo imagery, originally designed to measure terrain topography, have so far been little exploited for water applications, for instance for vehicle speed, wave speed and ocean current estimations (Matthews, 2005; Garay and Diner, 2007; Matthews and Awaji, 2010; De Michele et al., 2012). Kääb and Prowse (2011) exploit the time lag between the partner images of satellite stereo acquisitions to track river ice debris over time differences of around one minute and that way estimate for the first time two-dimensional ice and water-surface velocities over entire river reaches. They apply single stereo scenes over the St. Lawrence River and Mackenzie River from the Advanced Spaceborne Thermal Emission and Reflection Radiometer (ASTER) on board the NASA Terra spacecraft, from the Panchromatic Remote-sensing Instrument for Stereo Mapping (PRISM) on board the Japanese ALOS satellite, and from the Ikonos satellite. Here, we build upon their work and test the applicability of the method to an entire strip of ASTER scenes and demonstrate the type of information that could be retrieved from ice and water velocities over river reaches of several hundred kilometres. The focus of this study is therefore on exploring the methodology and not on an in-depth hydraulic analysis or the results.

2 Method

Our methodology consists of two key elements. Firstly, we observe ice debris on rivers, which is visible in high and medium resolution satellite images acquired during a certain time period after river ice break-up (Fig. 1 and Supplement). Such floating ice will under certain circumstances indicate surface-water velocities. Secondly, we exploit the fact that the two or more images forming along-track stereo data from a moving airborne or spaceborne platform are acquired by necessity with a temporal separation (Fig. 2 and Supplement), which is basically defined by the sensor travel speed above ground, and the base-to-height ratio of the system. For our study site over the Lena River in Siberia (Fig. 3), we apply a series of nine satellite stereo image pairs from ASTER with 15 m ground resolution and 55 s time lag.

2.1 Study site and data

The Lena River is one of the three largest Siberian rivers, with a length of ∼4260 km and a drainage area of $\sim 2.5 \times 10^6$ km^2 (Shiklomanov et al., 2006; Costard and Gautier, 2007). Its northward flow runs from the Baikal Mountains south of the Central Siberian Plateau to the Laptev Sea, bordering the Arctic Ocean. With a water discharge of about 520 km^3 yr^{-1} (ArcticRIMS, 2013) the Lena River plays an important role in the freshwater and sediment flux of the Arctic Ocean, contributing to about 15% of its total input (Costard and Gautier, 2007). Regular hydrological measurements have been conducted for over 70 yr by the Russian Hydrometeorological Services, collecting data such as discharge, ice thickness and freeze-up/break-up dates (Yang et al., 2002; Shiklomanov et al., 2006; ArcticRIMS, 2013). Minimum flows at the station Kusur (Fig. 4) are around 2000–5000 m^3 s^{-1} in winter, peaking rapidly to 80 000–120 000 m^3 s^{-1} during the annual spring flood (Shiklomanov et al., 2006; Costard and Gautier, 2007; ArcticRIMS, 2013). The observations show a low flow period between November and April and a peak discharge with maximum flow in May in the upstream regions, and in June downstream (Ye et al., 2003, 2009; Yang et al., 2007; ArcticRIMS, 2013). However, despite a good observational coverage throughout the whole river, the discharge measurements are much less accurate when river ice is present, the related error margin being between 15 and 30 % (Grabs et al., 1998; Shiklomanov et al., 2006).

The data set used in this study covers a reach of ∼ 620 km of the Lena River in its lower region between approximately 67°03′ N, 123°28′ E and 71°35′ N, 127°18′ E (Figs. 3 and 4). This reach is characterized by a wide riverbed with multiple channels separated by sand bars and vegetated alluvial islands in the south of the section studied. The river becomes narrower in the northern half of the study area, surrounded by rugged topography with elevations of up to 950 m a.s.l. At the southern end of the studied river reach, where Lena River enters our images, the water-surface level is at around 25 m a.s.l., at the northern downstream end about 5 m a.s.l., as indicated by a coarse DEM available for the region (Viewfinderpanoramas, 2013).

The ASTER instrument is an imaging spectro-radiometer onboard NASA's Terra platform, launched in December 1999. The sensor's 14 spectral bands are recorded using three subsystems using separate optical instruments: the Visible to Near-Infrared Radiometer (VNIR) with a 15m resolution, the Short-Wave-Infrared Radiometer (SWIR) with a 30 m resolution and the Thermal Infrared Radiometer (TIR) with a 90 m resolution. ASTER's stereo device (bands 3N and 3B), of particular interest for this study, is implemented in the VNIR subsystem that uses two independent telescopes. The nadir band (3N), with a spectral range of 0.76–0.86 µm (near infrared), is part of the three-spectral-band VNIR detector. The backward-looking telescope provides an along-track

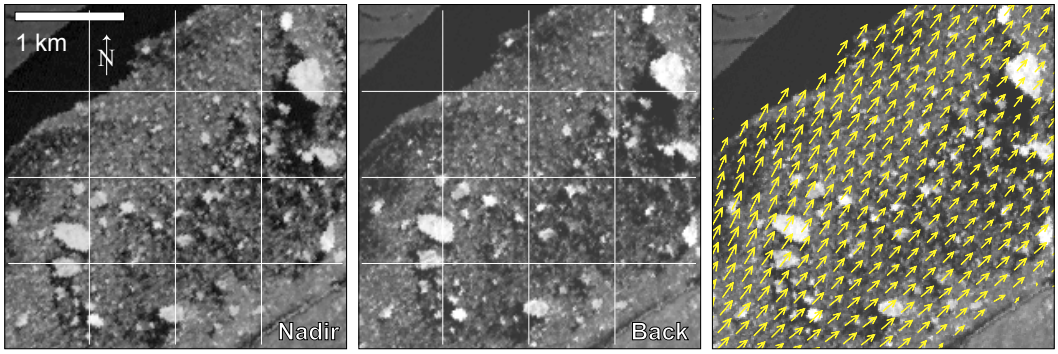

Fig. 1. Section of an ASTER nadir image (left) and an ASTER back-looking image (middle) acquired with 55 s time difference over Lena river at the southern margin of reach Fig. 8e. Right panel shows velocity vectors tracked by correlating the nadir and back-looking images. Displacement vectors are slightly exaggerated. Vector grid spacing is 165 m (11 ASTER pixels). Maximum ice-floe offsets are around 100 m (6.7 pixels; 1.8 m s^{-1}). The reference grid in the left and middle panel is meant to facilitate visual detection of river ice movement over the 55 s time lag.

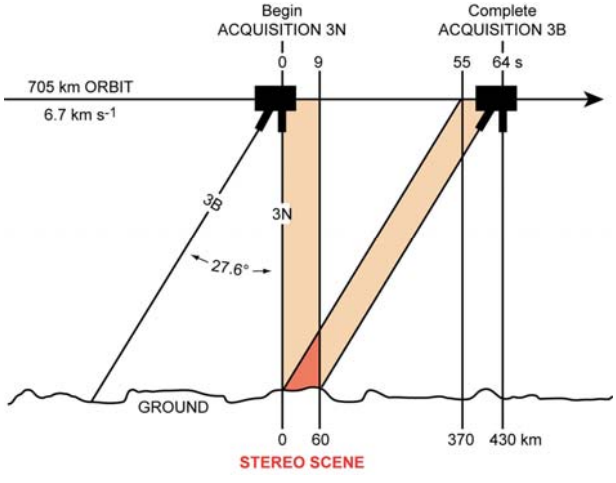

Fig. 2. Acquisition geometry of ASTER stereo. A 60 km-long and -wide scene is acquired from the nadir sensor (here used: near-infrared band 3N), and then 55 s later again from the back-looking near-infrared stereo sensor producing band 3B. Bands 3N and 3B together form a stereo scene.

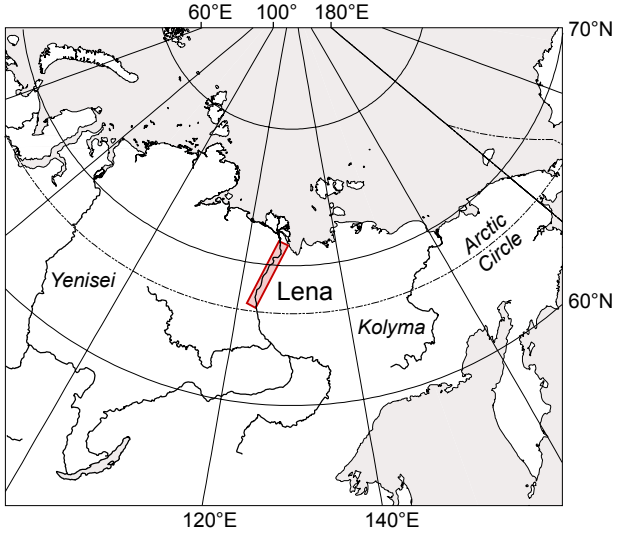

Fig. 3. Location of strip of nine ASTER stereo scenes of 27 May 2011 (red), used for ice and water velocities of Lena River, Siberia.

stereo-band (3B) with a tilt angle of 27.6° (30.9° if earth's curvature is taken into account) backwards from nadir, and the same spectral range and spatial resolution as the 3N band (Fig. 2). ASTER's image swath is approximately 60 km wide, being able to acquire data over the entire globe in a repeat period of 16 days (entire paragraph: Abrams et al., 2002). The time lag between the recordings of the 3N and 3B scenes is ∼ 55 s (Kääb and Prowse, 2011) (Figs. 1, 2 and Supplement).

In this study, we use nine continuous ASTER scenes taken on the 27 May 2011 (approx. 03:30 UTC), from a descending orbit: a north to south axis with an azimuth from approximately 205 to 200° from north (Figs. 3 and 4). The scenes cover in total about 32 400 km^2, of which roughly 2830 km^2 are river area at the time of acquisition. In contrast to Kääb and Prowse (2011), who had to rely on fortuitously acquired scenes found in the satellite data archives, the scenes of this study were acquired on demand for tracking river ice, and are to our best knowledge the first satellite stereo scenes specifically taken for such purpose.

No discharge and stage data are available to us for 2011 but the data available over 1936–2009 for Kusur (ArcticRIMS, 2013), at the northern end of the river reach studied, together with the river ice conditions found in the ASTER images and a satellite study by Pavelsky and Smith (2004), suggest that 27 May 2011 could exactly lie at the onset of the rapid annual rise of stage and discharge at Kusur, and that the more

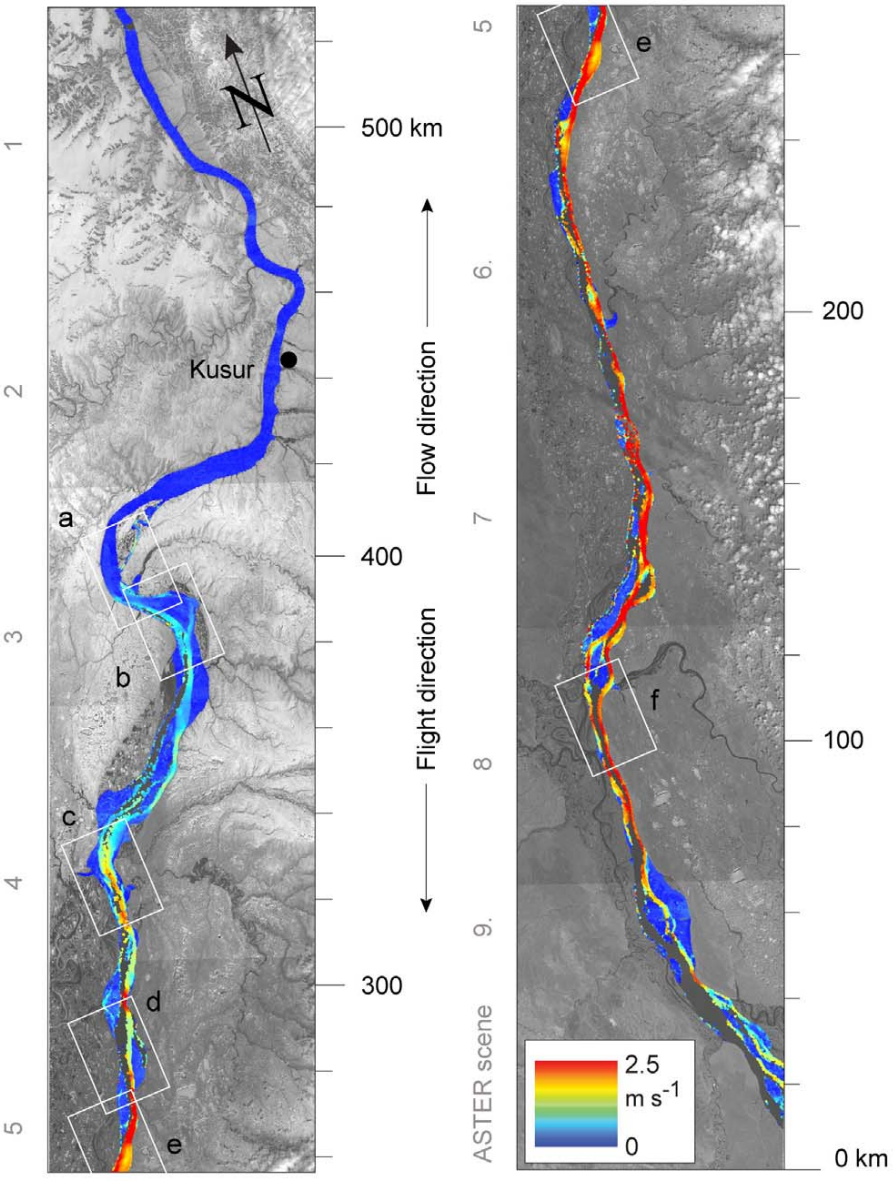

Fig. 4. Reach of Lena River studied. Ice speeds as of 27 May 2011 are corrected for stable-ground offsets and shown in colour code. The scale to the right indicates ASTER along-track coordinates. The numbers to the left indicate ASTER scenes 1–9. Rectangles with letters indicate the location of details Figs. 7 and 8.

southern parts of the reach under investigation are already under typical high-water conditions associated with spring flooding and river ice break-up (Pavelsky and Smith, 2004).

In order to also characterize typical low-water conditions, river outlines and sand bars are manually mapped using Landsat 7 scenes taken on 21 August 2011. The river parts visible on 21 August 2011 (Landsat) but not on 27 May 2011 (ASTER) are considered to indicate relatively shallow water on 27 May 2011. The only stage data available to us, for 2000 and 2008/2009 at Kusur, indicate minimum levels of around 3 m end of April and maximum levels of over 25 m at end of May to beginning of June. For mid to end August 2000 and 2008/2009 water levels are around 10 m (Shiklomanov et al., 2006; ArcticRIMS, 2013). Comparison to inundated areas from satellite images of other years suggests, however, that the 21 August 2011 water level could be considerably lower than the average for this time of the year.

2.2 Image processing

The ASTER back-looking images (3B) are co-registered to the nadir images (3N) using a first-order polynomial transformation, which is determined from tie points placed

on assumed stable areas at water-surface level along the river banks. The average root mean square (RMS) of co-registration residuals over the 9 scenes is 0.42 pixels (6.3 m). Both images, 3N and 3B are projected to the UTM-WGS84 coordinate system. The total elevation difference at water level is estimated using a 3 arc-second DEM, based on the 1 arc-second ASTER GDEM, and Russian 200 k and 100 k data (Viewfinderpanoramas, 2013). Over the 620 km of river the elevation difference at river surface is thus assessed to be not more than 20 m with an average altitude of around 11 m a.s.l., making scale variations in the image mosaic from absolute elevation and topographic distortions negligible and thus orthoprojection obsolete.

Ice-debris displacements are then tracked within each stereo pair, using the free software CIAS (Correlation Image AnalysiS; Kääb and Vollmer, 2000; Heid and Kääb, 2012; Kääb, 2013). This program uses a double normalized cross-correlation (NCC) operating in the spatial domain and based on the grey values of the images, to measure horizontal surface displacements with a precision of up to 1/8 of a pixel. For this matching, the nadir scene (3N) is considered as the reference image. An image block (reference template), the size of which is determined by the user, is searched for in the second image (3B), giving the difference in central pixel coordinates. Through tests, a reference template size of 11×11 pixels (165 m $\times$ 165 m) is found suitable for our study. Smaller templates produce more mismatches due to a reduction of feature uniqueness, whereas larger window sizes include too much river-ice deformation, thus decreasing the matching precision and leading to longer computing times (Debella-Gilo and Kääb, 2011b). After initial runs, a search window size of 20×20 pixels is chosen allowing for displacements of at least 150 m (10 pixels) to be found over the 55 s time lag. The output grid resolution is set to 11 pixels (165 m), identical to the reference template size, so that individual matches are independent, resulting in $\sim 130\,000$ measurements over the river and $\sim 550\,000$ outside within a coarse polygon surrounding the river. The raw displacements obtained with CIAS require post-processing and filtering to eliminate mismatches. Here, all measurements with a correlation coefficient below 0.6 are removed from the data set. The remaining data, displayed as vectors representing the magnitude and direction of the displacements (Fig. 1) is then inspected, any clearly aberrant results deleted manually, such as single vectors pointing upstream in disagreement with surrounding vectors. Further errors and gaps in the data are filtered out using a 3×3 moving window median filter. The final results are then converted to velocity, dividing the measured displacements through the time lag of 55 s between the stereo partners (Figs. 4, 7, 8).

2.3 Error budget

Three major sources of error affect our results:

i. co-registration errors between the 3N and 3B images;

ii. definition uncertainties of corresponding river ice features between the images;

iii. higher-order distortions in the satellite images.

(i.) Co-registration errors affect the displacements directly in the form of scene-specific translations, rotations and scales, because a first-order polynomial transformation between the stereo images is chosen here for a robust initial co-registration. Note that tie points in the 3N data and their correspondences in the 3B data are here measured manually, not through image matching, introducing thus further potential inaccuracy. In our case, a mean RMS error of under 0.5 pixels (equivalent to 7.5 m and 0.14 m s^{-1}) is indicated by the adjustments and considered acceptable.

(ii.) A number of factors related to the river ice features tracked will in reality reduce the theoretical matching precision of about 1/8 pixel of our algorithm (1.9 m, 0.03 m s^{-1}) (Debella-Gilo and Kääb, 2011a). River-ice aggregations might deform (geometric change) over the 55 s time interval, reducing the accuracy of NCC that is based on rigid image blocks (Debella-Gilo and Kääb, 2011b). River ice features might also change physically over 55 s such as from turning over, rotation, or emergence or sinking of ice floes at pixel or sub-pixel level, or apparently through bidirectional reflection effects (BRDF; spectral change) as the two stereo images are taken with a view angle difference of about 30° (Fig. 1). Quantification of this second category of errors is difficult as ice velocities would have to be known for strict validation. The closest approximation to assess the accuracy of matching moving river ice is to match consistently moving ice sections, and investigate the variation of matching results within an area limited enough to make ice deformations small or negligible. Several such tests are performed and give a standard deviation of around ± 2 m (0.04 m s^{-1}), a value very close to the assumed precision of our matching algorithm of 1/8 of a pixel, even when CIAS is modified to match with higher nominal precision than 1/8 pixel.

(iii.) The third category of errors stems from distortions and geometric noise in the images as yet not eliminated by the co-registration process, which is here based on a simple first-order polynomial transformation. ASTER data (and data from other sensors) are known to be subject to short-wavelength (so-called jitter) and long-wavelength spacecraft attitude angle variations that are not or not fully captured by the onboard measurement of these angles and lead therefore to pixel location errors (Leprince et al., 2007; Teshima and Iwasaki, 2008; Nuth and Kääb, 2011). As a special case for stereo applications, and thus our application, the results are not affected by the individual attitude error vectors of the 3N and 3B scenes, but rather by the vector sum of both error vectors. The individual errors from the two stereo partners could in extreme cases completely cancel or double each other by constructive or destructive interference, respectively.

Here, we attempt to investigate impacts from attitude angle errors by analysing offsets between the stereo images on

flat, stable-ground at river level (i.e. mainly in the floodplain). We measure offsets in these zones using the same matching parameters as for those on the river ice, and then rotate the ground coordinates of measurement locations and the x and y components of the offsets (both in UTM) by the track azimuth into a track coordinate system, so that along-track and cross-track components of distortions and noise can be investigated (Teshima and Iwasaki, 2008; Nuth and Kääb, 2011) (Figs. 4, 5). As this analysis is part of our overall method assessment, its results are contained in the following section.

3 Results and discussion

3.1 Image errors

The offsets over stable-ground around the Lena River (Fig. 5) are the combination of all of the above three error categories: (i) insufficient co-registration, (ii) errors from target definition, and (iii) higher-order errors from insufficiently corrected variations of attitude angles. The scatter of along-track and cross-track stable-ground offsets over the nine ASTER scenes has a mean of about 3 m (0.054 m s^{-1}) or of −6 m (0.11 m s^{-1}), respectively, and a standard deviation of ±10 m (±0.18 m s^{-1}) or ±6 m (±0.12 m s^{-1}) (Fig. 5). The stable-ground vector magnitudes (root sum square, RSS, of along-track and cross-track components) have a mean of 19 m (0.34 m s^{-1}) and a standard deviation of ±4 m (±0.08 m s^{-1}). We consider the standard deviation of stable-ground offsets of around ±0.08 m s^{-1} to be an initial estimate for the upper bound of the feasible velocity uncertainty of our method if only the mean land offset is subtracted from the river displacements.

The stable-ground offsets as shown in Fig. 5 have been obtained by averaging the along-track and cross-track offsets every 100 m using a running mean based on a 750 m window along the satellite path axis (black curves in Fig. 5). The power spectra of the along-track and cross-track offsets (insets in Fig. 5) suggest that the signals seen are composed of only a few dominant wavelengths. The dominant wavelengths in the cross-track offset variations are around 4.6 km (average amplitude 1 m), 34 km (avg. amplitude 5 m) and 60 km (avg. amplitude 3 m). In the along-track offsets the 4.6 km peak is very weak compared to the cross-track offsets, but the 34 km peak (avg. amplitude 5 m) is as strong as in the cross-track offsets. A peak in the along-track offsets can also be seen at ∼ 100 km wavelength (20 m amplitude).

Using running means of 4.5 km and 35 km (i.e. approx. the above dominant wavelengths from the power spectra) produces smoother versions of the signal that allow to better understand the nature of the variations (green and blue curves in Fig 5). Also given are the residual variations after subtracting the 4.5 km window running mean from the 750 m one (red curves in Fig. 5).

The profile data first of all exhibit some deficiencies of co-registration, for instance between scenes 4 and 5 in the along-track offsets, at around $x = 300$ km. Such deficiencies are well expected given the manual tie-point measurement and first-order polynomial fit used for co-registration. Part of the offset variations visible in the 35 km running means could in fact stem from imperfect co-registrations for the individual stereo pairs. In the same way, we attribute the ≥ 60 km wavelength variations to co-registration deficiencies.

The 4.5 km running mean, compared to the 35 km running mean exhibits clearly the ∼ 34 km wavelength of variations in both offset components, and the residuals with the 4.5 km running mean subtracted the ∼ 4.6 km wavelength in the cross-track component. Both these wavelengths are well known to potentially stem from imperfect measurement and correction of variations in sensor/spacecraft attitude angles (Leprince et al., 2007; Teshima and Iwasaki, 2008; Nuth and Kääb, 2011). However, we show here for the first time how these attitude angle errors vary over a series of scenes. Our data, in fact, suggest in particular a variation in amplitude of the ∼ 4.6 km jitter. (Note that the offsets we see are an overlay of the jitters in 3N and 3B, not the jitter of individual images).

The fact that the offset variations at 4.6 km, 34 km and > 60 km wavelength should stem from biases related to attitude angles and co-registration suggests that they will affect displacement measurements on stable ground and on the river in a similar way, and that they could thus be subtracted from the raw displacements. We consider a 750 m running mean (i.e. ∼ 1/6 of the 4.6 km wave) as appropriate for describing the offset variations of > 4.6 km. This choice is, however, certainly open to discussion, and also filters of other types than running means could be employed, such as frequency filters designed based on the above power spectra. Removing these statistically modelled offset biases (Teshima and Iwasaki, 2008; Nuth and Kääb, 2011), leaves a remaining scatter of about ± 9 m (∼ 1/2 pixel, ± 0.16 m s^{-1}; 1 standard deviation) that is then an estimate for the noise in individual displacement measurements to be expected after correcting effects from attitude angle variations and co-registration. This residual uncertainty considerably decreases when averaging the residual stable ground offsets over a number of points, for instance to ± 2.2 m (± 0.04 m s^{-1}) for 10 neighbouring points, or ± 1.5 m (± 0.03 m s^{-1}) for 20 points. A 750 m running mean over stable ground offsets after correction also shows a standard deviation of around ± 1.5 m, both in cross-track and along-track components. The combination of, on the one hand, averaging displacements, which will typically also be conducted for river ice displacements for a number of applications such as water discharge or ice flux estimates and, on the other hand, the above bias removal thus reduces the displacement uncertainty effectively to ∼ 1/8 of an ASTER pixel (i.e. around the estimated precision of the image matching).

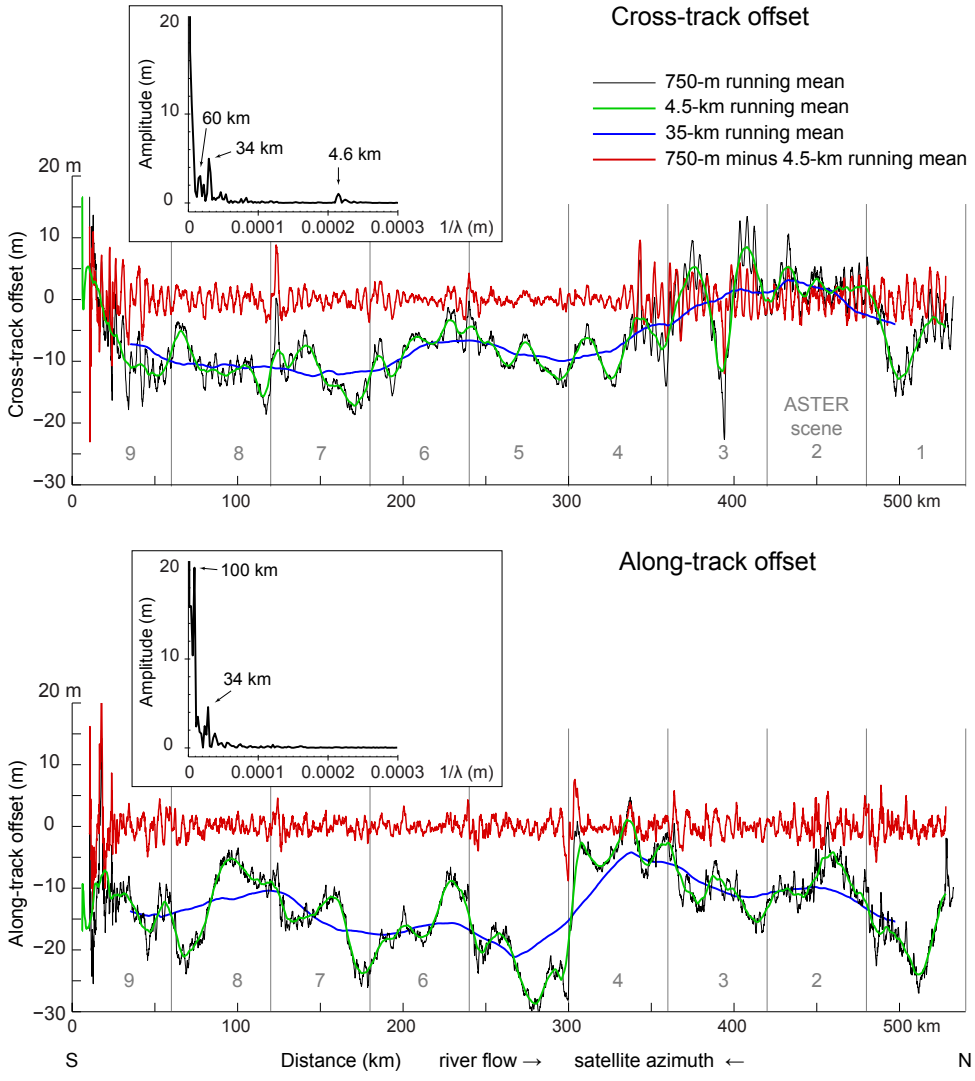

Fig. 5. Along-track profile of offsets between the nadir and back-looking data 3N and 3B on stable ground around the river. Offsets are shown as cross-track and along-track components. Black lines indicate offsets from a 750 m running mean, green from a 4.5 km running mean, and blue from a 35 km running mean. Red lines are the residual offsets if the 4.5 km running mean (green) is subtracted from the 750 m running mean (black). Insets show the power spectra of the 750 m running means, with most dominant wavelengths marked by arrows. The 4.6 km wavelength is well visible in the red line in the cross-track offset component, the 34 km wavelength in the green lines, and the 60 or 100 km wavelengths, respectively, in the blue lines.

Errors for the river remain then to the degree to which the biases from stable ground offsets are not representative for the offset biases over the river. We expect this difference, though, to be small and rather that the uncertainty remaining after removing offset biases is even less for river ice than for the stable ground around the river because (i) of less topographic distortions on the river, and because (ii) the matching targets around the river are typically less sharp than the river ice debris, which consists of exceptionally distinct contrast features.

3.2 Ice and water velocities

Figure 4 gives an overview over the entire river reach covered and the speeds obtained. Speeds shown are corrected for stable ground offsets as in Fig. 5. Highest ice debris speeds of up to around 2–2.5 m s^{-1} are observed at a number of places between 80 and 280 km of the south-to-north track coordinates (see also Fig. 6). From around 400 km northwards the river ice is jammed or not yet broken up. (From the images, the ice surface there is not homogenous but clearly a composite of individual ice floes). At many areas of the river plain, zero-displacements are found, either due to fast ice remains or on

sand bars, which are included in the displacements shown in Figs. 4, 7 and 8.

Figure 6 shows an along-track profile of ice speeds, topography, river width and ice area flux. For Fig. 6 all fast ice remains and sand bars have been excluded (in contrast to Figs. 4, 7 and 8 where they remain). The speeds in Fig. 6 are shown as uncorrected raw measurements and as 4.5 km running mean of measurements corrected for the stable ground offsets of Fig. 5. The speed profile, though, does not necessarily represent a profile of mean water velocities as it, first, includes velocities only where ice debris was present on the river and, second, as not at all sections ice velocities are considered to indicate water velocities (Figs. 7 and 8). The fact that Lena River flows not exactly long the ASTER azimuth leads to horizontal scale distortions with respect to the along-track coordinate system of Fig. 6. For a maximum off-track flow direction of $\sim 15°$ (e.g. from km 0 to 100) the scale error reaches 4 %, which is though considered negligible for the purpose of this study.

The topographic profile in Fig. 6 is computed by intersecting every displacement location in the river plain with the DEM from Viewfinderpanoramas (2013), which is compiled from the ASTER GDEM, and 200 k and 100 k Russian maps. A 4.5 km running mean is applied to the elevations in the same way as for the speeds. Surprisingly, at a first glance, the elevation profile shows parts where the river elevation is increasing with flow direction. This is due to the fact that sand bars, alluvial islands, etc. are included in our definition of the river plain and are thus also contained in the average elevation per 4.5 km bin. Essentially, the small-scale variations of the elevation profile in Fig. 6 reflect therefore the location of sand bars at or in the river as included in the DEM from Viewfinderpanoramas (2013).

The river width profile in Fig. 6 is based on the 21 August 2011 Landsat data (i.e. reflects low water conditions), not the 27 May 2011 conditions during which the displacements are measured. This choice is due to the fact that the ice/water velocity field mainly reflects the low water (=deep) river channels (Figs. 7 and 8, and discussion below). The water areas of 21 August 2011 (i.e. without banks, sand bars, islands, etc.) are gridded, the number of grid cells counted using an along-track 4.5 km running mean and the associated river area divided by 4.5 km to obtain an average width of all channels at individual along-track locations. The resulting mean river width, ranging from about 1.5 km to over 4 km, is also corrected for the angular difference between the ASTER track and the river direction.

The along-track variations of speed show a distinct 21 km wavelength variation (from power spectrum analysis) between local speed maxima, consistent for much of the 400 km river reach (Fig. 6). These undulations seem to be roughly positively correlated with the topographic undulations and, more pronounced, negatively correlated with the river width. Also the overall variation of speeds seems negatively correlated with the river width. Thus, speeds appear to be largest where the total channel width is smallest, which seems to be also, roughly, the locations of sand bars as indicated by local maxima of the elevation profile. These relations are well in line with hydraulic principles, but due to the low level of detail and vertical precision of the DEM available, and the methodological focus of this study, we have to leave open at this stage whether the 21 km undulations of ice speeds, and to a large extent presumably also water-surface speeds, are an effect of corresponding undulations in river slope (vertical effect) or variations in river width (horizontal effect), or both combined. Besides common processes of river sediment re-distribution, the permafrost surrounding of the river and, thus, the frozen river banks could also play a role (Costard and Gautier, 2007).

Multiplying the ice speeds of profile Fig. 6 with the number of measured flow field cells with ice and their area of $165\,\mathrm{m} \times 165\,\mathrm{m}$ and dividing the result by the length of the averaging window of 4.5 km gives some initial estimate of cross-sectional ice area fluxes along the river reach studied at the time of image acquisition, i.e. how much ice surface area passes a cross section per unit time (dashed line in Fig. 6). As this estimate does not consider variations in total ice volume per unit area, it is not an estimate of ice volume flux. Ice thickness and density variations are not easily obtained over entire river reaches. Variations of the fraction between water and ice debris are, however, estimated from the ASTER satellite data used. For each $165\,\mathrm{m} \times 165\,\mathrm{m}$ cell of the displacement grid the average digital number (DN) is extracted from the ASTER 3N image. The lowest DN obtained of the river reach is set to 0 % ice area density and the highest to 100 %. The percentage ice area density is then computed for each displacement grid cell and the above raw ice area flux corrected by multiplication with it (solid line in Fig. 6). The effect of this correction is large, reflecting the strong variations in ice surface area density along the reach and time of observation (Figs. 7 and 8). Ice area fluxes are shown using a 9 km running mean, instead of using a 4.5 km running mean as applied to the other data in Fig. 6, in order to reduce the additional noise inferred by the reflectance data used as indicator for ice debris density. Corrected ice area fluxes are up to $2000\,\mathrm{m^2\,s^{-1}}$. This distinct maximum at around 260 km is mainly due to high amounts and high density of ice, rather than due to particularly high ice speeds (Fig. 8e).

Figures 7 and 8 show close-ups (for locations see Fig. 4), typical for our results in terms of river ice conditions, river topography and flow, and measurements. The measurements shown are corrected for stable-ground offsets; measurements over fast ice remains and sand bars, etc. are included.

Figure 7, site a (see also Supplement panel a), presents the measurements at the onset of the ice jam, or not yet broken ice. Maximum ice velocities in front of the ice jam are up to $0.8\,\mathrm{m\,s^{-1}}$ with an abrupt decrease at the onset of the ice jam. We believe these highest speeds of ice debris to represent water velocities as the river ice debris there is sparse and unconnected (Fig. 7, site a, left panel) (only wind drag

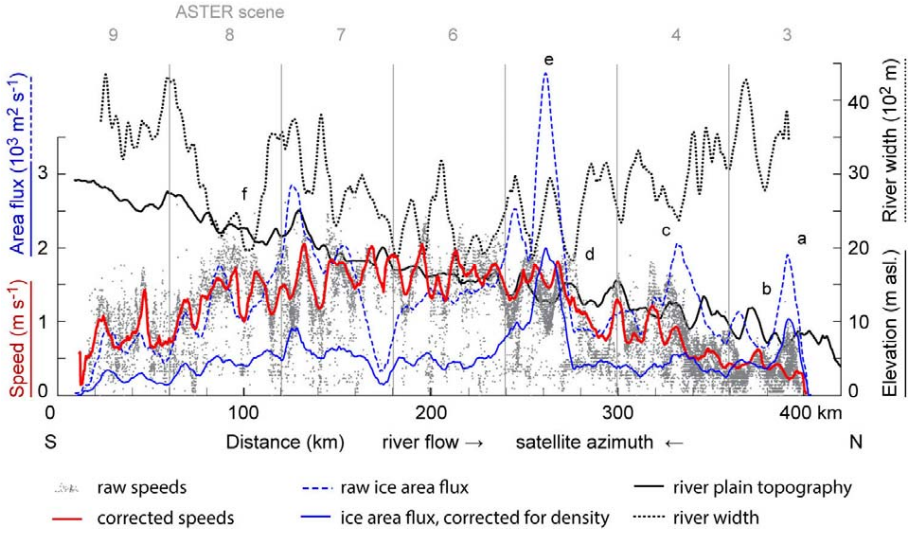

Fig. 6. Along-track profile of ice speeds, ice area fluxes, river width and river plain elevation; 4.5 km running means for speeds, topography and width, 9 km for area fluxes. Ice speeds (red) are given without (dashed) and with stable ground offsets corrected (solid). Ice area fluxes are calculated as a product of ice speed and cross-section width that contains ice debris (blue dashed). Ice area fluxes are also corrected for ice density as obtained from the reflectance variations in the ASTER scenes (solid blue). River plain elevation is interpolated from a DEM compiled from the ASTER GDEM and Russian topographic maps (www.viewfinderpanoramas.org). Lower-case letters indicate the location of sites of Figs. 4, 7 and 8.

could then cause deviations between ice and water velocities). Even after the abrupt speed decreases at the onset of the ice jam there is still statistically significant deformation of the ice over most of the channel width along further 13 km, with a clear shear margin to the lateral fast ice. Interestingly, and in contrast to the other river sections described below, the zones of highest speeds at site a correspond not well with the areas of assumed large water depths, which are areas that are also under water in the 21 August 2011 Landsat scenes (sand bars and other areas above the water level on 21 August 2011 but not on 27 May 2011 are outlined in the figures). This clearly reflects the upstream damming effect of the ice jam that decelerates ice debris first in the centre of the river.

Figure 7, site b (see also Supplement panel b), is located just upstream of site a, without obvious influence by the ice jam. Maximum speeds reach up to 1.2 m s^{-1} for some few locations, mostly up to 0.8 m s^{-1}. At site b, Lena River has two main branches and the pattern of speeds coincides well with water depths as reflected in the 21 August 2011 sand bars. Sand bars of 21 August 2011 have been classified in bare ones (solid outlines) and ones with vegetation (dashed outlines), the latter of which should reflect even lower water depths than over the bare sand bars if we assume that the presence of vegetation indicates least flooding and river ice impact.

Figure 7, site c (see also Supplement panel c), shows the measurement results at around 330 km. This is a reach where Lena River opens up from a narrower to a wider channel. This divergence is well reflected by a widening of the velocity field along with a decrease of maximum speeds from about 1.7 m s^{-1} to 0.8 m s^{-1}. The loose and unconnected ice debris suggests that ice velocities at site c largely reflect water velocities. Again, the location of bare and vegetated sand bars corresponds well with the pattern of speeds.

Figure 7, site d (see also Supplement panel d), shows a reach with little ice debris in the main channel and thus certainly only a limited representative flow field measurement. Speeds reach to over 2 m s^{-1} upstream of the central sand bar, 0.9 m s^{-1} at the sand bar, and again up to almost 2 m s^{-1} downstream of it. Site d is a good illustration of the 21 km undulations of speed maxima (Fig. 6).

In contrast to site d, Fig. 7, site e (see also Supplement panel e), shows a reach with almost complete cover by ice debris and thus a very complete velocity field. Overall speeds correspond well with the channel width, with maximum speeds of up to 2.3 m s^{-1} at the narrowest sections above and below the central sand bar, at which speeds reach up to 1.7 m s^{-1}. Lowest speeds in the channel of 1.2 m s^{-1} are found over and downstream of the central sandbar – besides at the channel margins. Again, site e well demonstrates the 21 km wavelength undulations of ice/water speed.

Figure 7, site f (see also Supplement panel f), shows an example where Lena river splits up in two channels. Speeds reach up to 2 m s^{-1} and decrease at two sand bar locations, to the south and the north of site f.

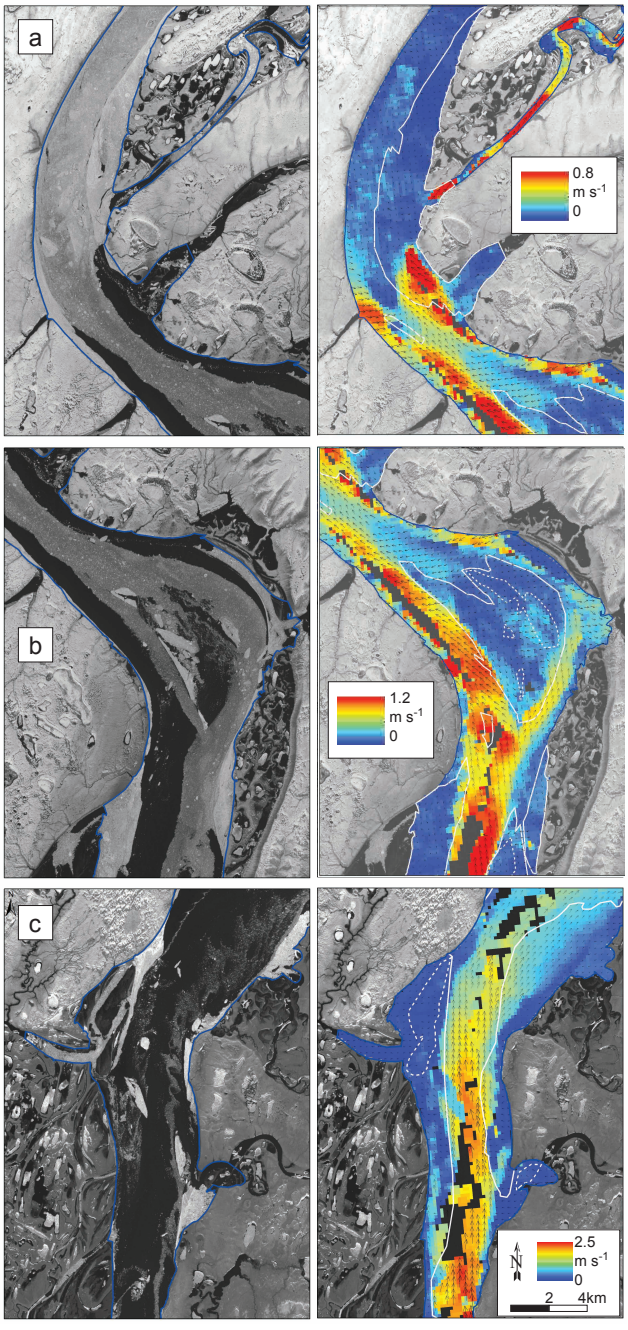

Fig. 7. Raw ASTER satellite imagery of 27 May 2011 used for ice tracking (left column) and velocity fields measured (right column). Sand bars (solid white lines) and vegetated islands (dotted white lines) from low-water conditions as of 21 August 2011. Speeds are colour coded. Velocity vectors (originally a 165 m × 165 m grid) are resampled to a 330 m × 330 m grid for better visibility. For locations of sites (lower-case letters) see Figs. 4 and 6.

4 Conclusions

For the first time, we present two-dimensional river ice velocities – presumably to a large extent water velocities – over a reach of several hundred kilometres. The data over the lower part of Lena River, Siberia, stem from – also for the first time – satellite data especially acquired for this purpose. We successfully exploit the ∼ 1 min. time lag between satellite stereo images to track river ice debris over this period.

We demonstrate that one can through careful modelling of image distortions and noise achieve displacement accuracies of far below the pixel size of the images used, here 15 m for the ASTER stereo channels. Combined with spatial averaging of even only a few raw displacements, displacement accuracy approaches the precision limit of image matching, assumed to be around 1/8 of a pixel in our study. Besides the correction of image and sensor errors, this high accuracy is also a result of the almost perfect visual contrast caused by ice floes, and by the planar topography of water surfaces that limits effects from topographic distortions.

The two main data errors found stem from imperfect co-registration of the stereo images, and errors connected to sensor/spacecraft attitude angles. Co-registration as done in our study, through manually collected tie points, could certainly be improved, for instance by automatic matching of tie points. Though, as co-registration will in any case be contaminated by higher-order sensor errors, it remains questionable to what extent common co-registration could be perfect, unless a geometric model is developed and employed that includes all these sensor errors. Our approach here was thus rather to perform an initial robust co-registration using a first-order polynomial model, and correct higher-order terms later in the results by statistical methods.

In our investigation of ASTER image distortions due to errors connected to attitude angles, we identify two dominant wavelengths, about 35 km and 4.5 km (jitter), confirming earlier analyses on the same problem (Leprince et al., 2007; Teshima and Iwasaki, 2008; Nuth and Kääb, 2011) and in line with unpublished results from ASTER science team tests. In contrast to these earlier studies, however, we analyse a series of nine ASTER scenes. While we find no clear variation in the roughly ± 10 m amplitude for the 35 km wavelength distortion, the ∼ 4.5 km wavelength jitter (frequency about 1/13 per 60 km ASTER scene) clearly varies in amplitude from almost zero to up to about ± 2.5 m in horizontal projection. As these distortions are estimated within stereo partners, and without being able to attribute them to individual images (Teshima and Iwasaki, 2008; Nuth and Kääb, 2011), the amplitude variations could well be due to tiny phase shifts between the two individual wave components from the 3N and 3B scenes that are able to shift the wave sum from a constructive to a destructive regime and vice-versa. From such a process it would then be well expected that the interference of shorter wavelengths (here ∼ 4.5 km) is much more affected than longer wavelenghts (here ∼ 35 km).

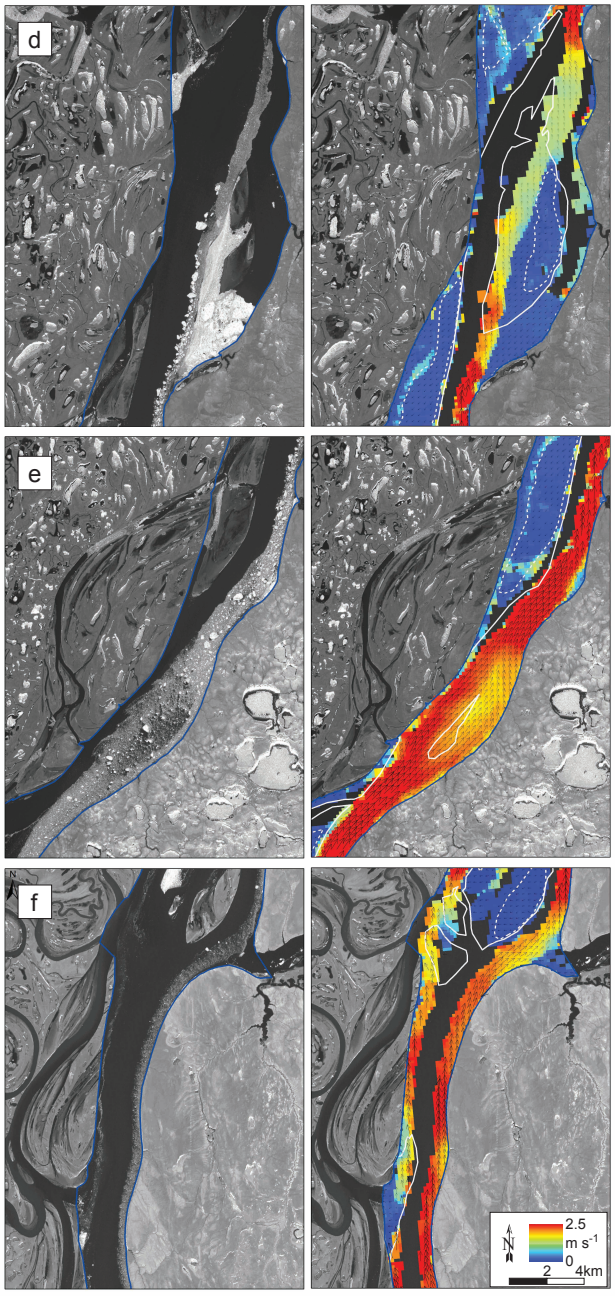

Fig. 8. Raw ASTER satellite imagery of 27 May 2011 used for ice tracking (left column) and velocity fields measured (right column). Sand bars (solid white lines) and vegetated islands (dotted white lines) from low-water conditions as of 21 August 2011. Speeds are colour coded. Velocity vectors (originally a 165 m × 165 m grid) are for resampled to a 330 m × 330 m grid better visibility. For locations of sites (lower-case letters) see Figs. 4 and 6.

Over the Lena River reach studied, maximum ice/water speeds reach up to 2.5 m s^{-1} on 27 May 2011 (03:30 UTC), with a clear undulation of average speeds with a wavelength of about 21 km and amplitude of up to around ± 0.5 m s^{-1}. Speed variations are negatively correlated with river width and, roughly, positively with the frequency of topographic undulations associated with sand bars along the river reach.

Our river ice flow field clearly shows the potential and the limitations of our approach. While we were able to derive surface velocities with sub-pixel accuracy (up to roughly ± 0.04 m s^{-1} for ASTER), the approach relies on the presence of river ice debris. The flow field might thus not cover the entire river width (cf. Kääb and Prowse, 2011). Also, this requirement limits the approach to times where such ice debris is visible on the river (i.e. a few days, or weeks in maximum, before freezing up and after ice break-up). The movement of river ice cannot under all circumstances be safely assumed to indicate water velocities. Though, our approach can in any case be used to investigate processes related to river ice, such as ice fluxes or ice jamming. While we demonstrate here only surface motion data, products with added value for hydrological, hydraulic or geomorphologic studies can be obtained by combining the motion data with data such as water levels or river discharges, or riverbed riverbed bathymetry (Beltaos and Kääb, 2013).

So far, satellite stereo missions, typically designed for topographic mapping, are not targeting rivers during freeze-up or ice break-up. Rather, acquisition plans often omit these seasons to avoid snow cover that limits the usefulness of optical stereo data for DEM extraction due to lack in visual contrast. Our study demonstrates the potential of targeting rivers at these two seasons. The chances for successful acquisitions of suitable stereo data are, however, considerably limited. First, optical data are generally dependent on clear-sky day-time conditions. Second, the typical repeat cycles of sensors such as ASTER or PRISM of roughly 14 days to a month bear a considerable probability that suitable river ice conditions are completely missed for an entire season. However, high-resolution missions of single sensors or sensor constellations, such as Ikonos, Quickbird, WorldView, Pleiades etc., with potential repeat times of few days, minimize this risk and at the same time promise with their pixel resolutions of down to 0.5 m a velocity accuracy on the order of up to 0.001 m s^{-1} (Kääb and Prowse, 2011). The high costs associated with programming such, typically commercial, satellites might in most cases restrict their employment for river ice velocities on applications related to hazard management, such as flooding due to ice jams, river engineering or other construction works. A new category of satellite data suitable for tracking river ice could come in the near future from constellations of small satellites carrying video or high-frequency imaging sensors such as those planned by the companies Skybox imaging and Planet labs.

Supplementary material related to this article is available online at http://www.hydrol-earth-syst-sci.net/17/4671/2013/hess-17-4671-2013-supplement.zip.

Acknowledgements. Acquisition of the ASTER images was guided by NASA JPL, through the ASTER science team and the Global Land Ice Measurements from Space (GLIMS) initiative. For the research leading to these results A. Kääb has received funding from the European Research Council under the European Union's Seventh Framework Programme (FP/2007-2013) / ERC grant agreement no. 320816. M. Lamare was funded through the ESA project Glaciers_ cci (4000101778/10/I-AM). His work was conducted during an internship at the University of Oslo as part of his studies at SIGMA of the University of Toulouse 2 Le Mirail/ENSAT. The work of A. Kääb and M. Lamare is also a pre-study for the Z-Earth mission proposal (http://www.legos.obs-mip.fr/recherches/missions-satellites/z-earth). Work by M. Abrams was performed at the Jet Propulsion Laboratory/California Institute of Technology under contract to the National Aeronautics and Space Administration. We are grateful to Jonathan de Ferranti for the background DEM, which we obtained from http://www.viewfinderpanoramas.org. Hydrological data were obtained from http://rims.unh.edu/.

Author contributions: A. Kääb designed and overlooked the study, did data analysis and wrote the paper. M. Lamare performed the image processing, prepared the results and wrote the paper. M. Abrams lead acquisition of the ASTER data and edited the paper.

Edited by: A. Loew

References

Abrams, M., Hook, S., and Ramachandran, B.: ASTER User Handbook. Version 2, Jet Propulsion Laboratory, California Institute of Technology, 2002.

ArcticRIMS: A regional, integrated hydrological monitoring system for the pan-Arctic land mass, http://rims.unh.edu/, 2013.

Beltaos, S. and Kääb, A.: River discharge during ice breackup from satellite imagery, Cold Reg. Sci. Technol., 98, 35–46, doi:10.1016/j.coldregions.2013.10.010, 2013.

Bjerklie, D. M., Dingman, S. L., Vorosmarty, C. J., Bolster, C. H., and Congalton, R. G.: Evaluating the potential for measuring river discharge from space, J. Hydrol., 278, 17–38, doi:10.1016/S0022-1694(03)00129-X, 2003.

Bjerklie, D. M., Moller, D., Smith, L. C., and Dingman, S. L.: Estimating discharge in rivers using remotely sensed hydraulic information, J. Hydrol., 309, 191–209, doi:10.1016/j.jhydrol.2004.11.022, 2005.

Costard, F. and Gautier, E.: The Lena River: hyrdomorphodynamic features in a deep permafrost zone, in: Large Rivers. Geomorphology and Mangement, edited by: Gupta, A., John Wiley and Sons Ltd., West Sussex, England, 225–234, 2007.

De Michele, M., Leprince, S., Thiebot, J., Raucoules, D., and Binet, R.: Direct measurement of ocean waves velocity field from a single SPOT-5 dataset, Remote. Sens. Environ., 119, 266–271, doi:10.1016/j.rse.2011.12.014, 2012.

Debella-Gilo, M. and Kääb, A.: Sub-pixel precision image matching for measuring surface displacements on mass movements using normalized cross-correlation, Remote Sens. Environ., 115, 130–142, doi:10.1016/j.rse.2010.08.012, 2011a.

Debella-Gilo, M. and Kääb, A.: Locally adaptive template sizes in matching repeat images of Earth surface mass movements, ISPRS J Photogramm, 69, 10–28, doi:10.1016/j.rse.2010.08.012, 2011b.

Garay, M. J. and Diner, D. J.: Multi-angle Imaging SpectroRadiometer (MISR) time-lapse imagery of tsunami waves from the 26 December 2004 Sumatra-Andaman earthquake, Remote Sens. Environ., 107, 256–263, doi:10.1016/j.rse.2006.10.022, 2007.

Gerard, R. L. and Davar, K. S.: Introduction, in: River Ice Jams, edited by: Beltaos, S., Water Resources Rublication, LLC Highlands Ranch, CO, 1–28, 1995.

Grabs, W. E., Fortmann, F., and De Couuel, T.: Discharge observation networks in Arctic regions: Computation of the river runoff into the Arctic Ocean, its seasonality and variability, The Freshwater Budget of the Arctic Ocean, Tallin, 249–268, 1998.

Heid, T. and Kääb, A.: Evaluation of existing image matching methods for deriving glacier surface displacements globally from optical satellite imagery, Remote Sens. Environ., 118, 339–355, doi:10.1016/j.rse.2011.11.024, 2012.

Jasek, M. and Beltaos, S.: Ice-jam release: javes, ice runs and breaking fronts, in: River Ice Breakup, edited by: Beltaos, S., Water Resources Rublication, LLC Highlands Ranch, CO, 247–303, 2008.

Kääb, A. and Vollmer, M.: Surface geometry, thickness changes and flow fields on creeping mountain permafrost: automatic extraction by digital image analysis, Permafrost Periglac, 11, 315–326, 2000.

Kääb, A. and Prowse, T.: Cold-regions river flow observed from space, Geophys. Res. Lett., 38, L08403, doi:10.1029/2011GL047022, 2011.

Kääb, A.: Correlation Image Analysis software (CIAS), http://www.mn.uio.no/icemass, 2013.

Leprince, S., Barbot, S., Ayoub, F., and Avouac, J. P.: Automatic and precise orthorectification, coregistration, and subpixel correlation of satellite images, application to ground deformation measurements, Ieee T. Geosci. Remote, 45, 1529–1558, doi:10.1109/Tgrs.2006.888937, 2007.

Matthews, J.: Stereo observation of lakes and coastal zones using ASTER imagery, Remote Sens. Environ., 99, 16–30, doi:10.1016/j.rse.2005.04.029, 2005.

Matthews, J. P. and Awaji, T.: Synoptic mapping of internal-wave motions and surface currents near the Lombok Strait using the Along-Track Stereo Sun Glitter technique, Remote Sens. Environ., 114, 1765–1776, doi:10.1016/j.rse.2010.03.007, 2010.

Mermoz, S., Allain, S., Bernier, M., Pottier, E., and Gherboudj, I.: Classification of river ice using polarimetric SAR data, Can. J. Remote Sens., 35, 460–473, 2009.

Nuth, C. and Kääb, A.: Co-registration and bias corrections of satellite elevation data sets for quantifying glacier thickness change, Cryosphere, 5, 271–290, 2011.

Pavelsky, T. M. and Smith, L. C.: Spatial and temporal patterns in Arctic river ice breakup observed with MODIS and AVHRR time series, Remote Sens. Environ., 93, 328–338, doi:10.1016/j.rse.2004.07.018, 2004.

Peterson, B. J., Holmes, R. M., McClelland, J. W., Vorosmarty, C. J., Lammers, R. B., Shiklomanov, A. I., Shiklomanov, I. A., and Rahmstorf, S.: Increasing river discharge to the Arctic Ocean, Science, 298, 2171–2173, 2002.

Prowse, T. D.: Environmental significance of ice to streamflow in cold regions, Freshwater Biol., 32, 241–259, doi:10.1111/j.1365-2427.1994.tb01124.x, 1994.

Prowse, T. D. and Culp, J. M.: Ice breakup: a neglected factor in river ecology, Can. J. Civil Eng., 30, 128–144, doi:10.1139/L02-040, 2003.

Prowse, T. D.: River-ice hydrology, in: Encyclopedia of Hydrological Sciences, edited by: Anderson, M. G., John Wiley and Sons Ltd., West Sussex, England, 2657–2677, 2005.

Prowse, T. D., Bonsal, B., Duguay, C. R., Hessen, D. O., and Vuglinsky, V. S.: River and lake ice, in: Global Outlook for Ice and Snow, United Nations Environment Programme, 201–214, 2007.

Romeiser, R., Runge, H., Suchandt, S., Sprenger, J., Weilbeer, H., Sohrmann, A., and Stammer, D.: Current measurements in rivers by spaceborne along-track InSAR, Ieee T. Geosci. Remote, 45, 4019–4031, doi:10.1109/Tgrs.2007.904837, 2007.

Romeiser, R., Suchandt, S., Runge, H., Steinbrecher U., and Grünler, S.: First analysis of TerraSAR-X along-track InSAR-derived current fields, Ieee T. Geosci. Remote, 48, 820–829, doi:10.1109/Tgrs.2009.2030885, 2010.

Shiklomanov, A. I., Yakovleva, T. I., Lammers, R. B., Karasev, I. P., Vorosmarty, C. J., and Linder, E.: Cold region river discharge uncertainty – estimates from large Russian rivers, J. Hydrol., 326, 231–256, doi:10.1016/j.jhydrol.2005.10.037, 2006.

Siegmund, R., Bao, M. Q., Lehner, S., and Mayerle, R.: First demonstration of surface currents imaged by hybrid along- and cross-track interferometric SAR, Ieee T. Geosci. Remote, 42, 511–519, doi:10.1109/Tgrs.2003.817816, 2004.

Smith, L. C.: Satellite remote sensing of river inundation area, stage, and discharge: A review, Hydrol. Process, 11, 1427–1439, 1997.

Smith, L. C.: Emerging applications of interferometric synthetic aperture radar (InSAR) in geomorphology and hydrology, Ann. Assoc. Am. Geogr., 92, 385–398, 2002.

Smith, L. C. and Pavelsky, T. M.: Estimation of river discharge, propagation speed, and hydraulic geometry from space: Lena River, Siberia, Water Resour. Res., 44, W03427, doi:10.1029/2007wr006133, 2008.

Teshima, Y. and Iwasaki, A.: Correction of attitude fluctuation of terra spacecraft using ASTER/SWIR imagery with parallax observation, Ieee T. Geosci. Remote, 46, 222–227, doi:10.1109/Tgrs.2007.907424, 2008.

Unterschultz, K. D., van der Sanden, J., and Hicks, F. E.: Potential of RADARSAT-1 for the monitoring of river ice: Results of a case study on the Athabasca River at Fort McMurray, Canada, Cold Reg. Sci. Technol., 55, 238–248, doi:10.1016/j.coldregions.2008.02.003, 2009.

Viewfinderpanoramas: http://www.viewfinderpanoramas.org, 2013.

Vincent, F., Raucoules, D., Degroeve, T., Edwards, G., and Mostafavi, M. A.: Detection of river/sea ice deformation using satellite interferometry: limits and potential, Int. J. Remote Sens., 25, 3555–3571, doi:10.1080/01431160410001688303, 2004.

White, K. D. and Beltaos, S.: Development of ice-affected satge-frequency curves, in: River Ice Breakup, edited by: Beltaos, S., Water Resources Rublication, LLC Highlands Ranch, CO, 305–348, 2008.

Yang, D. Q., Kane, D. L., Hinzman, L. D., Zhang, X. B., Zhang, T. J., and Ye, H. C.: Siberian Lena River hydrologic regime and recent change, J. Geophys. Res.-Atmos., 107, 4694, doi:10.1029/2002jd002542, 2002.

Yang, D. Q., Zhao, Y. Y., Armstrong, R., Robinson, D., and Brodzik, M. J.: Streamflow response to seasonal snow cover mass changes over large Siberian watersheds, J. Geophys. Res.-Earth., 112, F02s22, doi:10.1029/2006jf000518, 2007.

Ye, B. S., Yang, D. Q., and Kane, D. L.: Changes in Lena River streamflow hydrology: Human impacts versus natural variations, Water Resour. Res., 39, 1200, doi:10.1029/2003wr001991, 2003.

Ye, B. S., Yang, D. Q., Zhang, Z. L., and Kane, D. L.: Variation of hydrological regime with permafrost coverage over Lena Basin in Siberia, J. Geophys. Res.-Atmos., 114, D07102, doi:10.1029/2008jd010537, 2009.